

Imaginary Gauge-steerable Edge Modes In Non-Hermitian Aubry-André-Harper Model

Yazhuang Miao,¹ Wei Ding,¹ Litong Wang,¹ Xiaolong Zhao*,¹ Shengguang Liu^{†,1} and Xuexi Yi^{‡2}

¹*School of Science, Qingdao University of Technology, Qingdao, Shandong, China*

²*Center for Quantum Sciences and School of Physics,*

Northeast Normal University, Changchun, Jilin, China

(Dated: January 13, 2026)

We investigate a non-Hermitian Aubry-André-Harper lattice exhibiting quasiperiodicity, featuring an imaginary gauge field that varies spatially but averages to zero. In the presence of open boundary conditions, this system is precisely mapped, through a nonunitary gauge transformation, to the Hermitian AAH model with balanced hopping terms. The mapping leaves the spectrum unchanged but reshapes each eigenfunction by a realization-dependent random-walk envelope. In a parameter regime where the Hermitian counterpart hosts spectrally isolated in-gap boundary modes, we identify two such modes with sharply different responses to the envelope: one stays anchored at the boundary, while the other is controllable via the gauge, allowing its peak intensity to be relocated solely by altering the gauge setup without modifying the associated eigenenergy. Additionally, we demonstrate that this steerable mode can be preferentially enhanced and generated from an initial bulk wavefunction by introducing mild site-specific amplification at a location determined exclusively from the Hermitian model using the biorthogonal function. These findings offer pathways for both static and dynamic manipulation of spatially adjustable in-gap states in quasiperiodic non-Hermitian lattices.

I. INTRODUCTION

Non-Hermitian Hamiltonians offer an effective framework for describing driven or open quantum systems characterized by gain and loss, leakage, measurement backaction, or nonreciprocal couplings. These systems support phenomena that have no counterparts in Hermitian regimes, including parity-time-symmetry breaking, exceptional points, and topological structures of complex spectra [1–13]. In lattice systems, non-Hermiticity disrupts the conventional bulk-boundary correspondence and localization behaviors, thereby facilitating boundary-state accumulation, amplification, and wave manipulation that transcend Hermitian frameworks [14, 15].

A hallmark manifestation of non-Hermiticity in lattice systems is the non-Hermitian skin effect (NHSE). Under open boundary conditions (OBC), a macroscopic number of eigenstates become exponentially localized near the boundaries, in stark contrast to the delocalized Bloch waves supported by the same system under periodic boundary conditions (PBC). This pronounced sensitivity to boundary conditions underscores the breakdown of conventional Bloch band theory and has motivated the development of generalized bulk-boundary correspondences based on non-Bloch band theory and point-gap topology [16–22]. The NHSE and its consequences for boundary spectra and experimentally accessible signatures have been extensively explored [12–15].

Imaginary gauge fields provide an alternative approach to non-Hermitian localization that does not require uniform nonreciprocity. In the Hatano-Nelson model, a uniform imaginary vector potential alters the localization properties and induces a pronounced sensitivity to boundary conditions [23, 24]. More recently,

Longhi demonstrated that strong skin-like localization can emerge solely from spatial fluctuations in the imaginary gauge field profile, even when the spatial average of the imaginary gauge field vanishes, thereby rendering the lattice globally reciprocal [25]. In the erratic non-Hermitian skin effect (ENHSE), the eigenstates exhibit an effective random-walk envelope, with localization centers determined by the extrema of the corresponding cumulative gauge field. This mechanism is distinct from both the conventional non-Hermitian skin effect, arising from net nonreciprocity, and Anderson localization. Within this framework, a question arises about how boundary-localized in-gap modes respond when such erratic gauge fluctuations are incorporated into quasiperiodic structures.

Quasiperiodic lattices provide a controlled setting in which localization and spectral gaps arise without uncorrelated disorder. The Aubry-André-Harper (AAH) model serves as the paradigmatic example, featuring a self-dual localization transition [26] and is closely connected to the Harper equation and the Hofstadter problem [27–29]. Under OBC, the bulk energy gaps of the AAH spectrum can host spectrally isolated in-gap modes that are localized near the system boundaries, with their existence and spatial profiles depending on the quasiperiodic phase offset [30–32]. Experimental realizations of quasiperiodic localization and gap physics have been reported in photonic and cold-atom platforms [33–37]. Non-Hermitian extensions of AAH-type models, incorporating nonreciprocal hopping, complex quasiperiodic potentials, or pairing terms, have been demonstrated to alter localization properties and induce anomalous boundary or skin modes [38–43]. In contrast, the response of in-gap boundary-localized modes to a spatially fluctuating imaginary gauge field with zero mean (corresponding

to the erratic-gauge regime) remains largely unexplored.

These developments leave a specific gap: while quasiperiodic AAH chains can host spectrally isolated in-gap modes localized near open boundaries. However, the behavior of such boundary-localized in-gap modes remains unexplored when the hopping asymmetry arises from a zero-mean but strongly fluctuating imaginary gauge field-termed the erratic-gauge regime. In this work, we address this problem by employing an exact site-dependent nonunitary gauge transformation under OBC. This transformation maps the non-Hermitian chain onto its Hermitian AAH counterpart, preserving the open-boundary spectrum. The mapping shows that gauge fluctuations do not shift eigenvalues but reshape right/left eigenfunctions through a realization-dependent random-walk envelope. Within spectral gaps we identify two isolated boundary-localized modes with sharply different sensitivity to this envelope: one remains pinned to the boundary, whereas the other is gauge-steerable, allowing its probability maximum to be repositioned solely by varying the gauge realization without altering its eigenvalue. Furthermore, we propose a practical preparation protocol leveraging weak local gain. The gain site is determined once from the profile of the corresponding Hermitian mode and can then be fixed across different gauge realizations to selectively amplify the steerable in-gap mode from an initial bulk wave packet.

The remainder of the paper is organized as follows. In Sec. II, the continuum and tight-binding models with Bernoulli gauge disorder is introduced. In Sec. III, the nonunitary gauge transformation is derived under OBC and used to analyze the Lyapunov exponents and the phase diagram is presented. In Sec. IV, we show the co-existence of pinned and steerable in-gap modes and verify this by finite-size diagnostics. In Sec. V, we propose a weak local-gain protocol and demonstrate the dynamical preparation of the gauge-steerable mode. Finally, we conclude in Sec. VI.

II. MODEL

A particle of mass m moving in a one-dimensional bichromatic lattice subjected to an imaginary gauge field can be described by the continuum Hamiltonian

$$H_{\text{cont}} = \frac{(p - i\hbar A(x))^2}{2m} + V_1 \sin^2(k_1 x) + V_2 \cos(2k_2 x + \varphi), \quad (1)$$

where $p = -i\hbar\partial_x$ is the momentum operator, $A(x) \in \mathbb{R}$ is a prescribed spatial profile (with dimension of inverse length), $V_{1,2}$ are the lattice depths, and $k_{1,2}$ are the wave numbers of the primary and secondary lattices, respectively. The phase φ sets the spatial offset of the secondary lattice. We consider an open interval of space, introducing $X(x) = \int_{x_0}^x A(x') dx'$, so that $X'(x) = A(x)$. Using $e^{-X} p e^X = p - i\hbar X'(x)$, one obtains $e^X (p - i\hbar A) e^{-X} = p$ and hence the nonunitary gauge-transformed Hamilto-

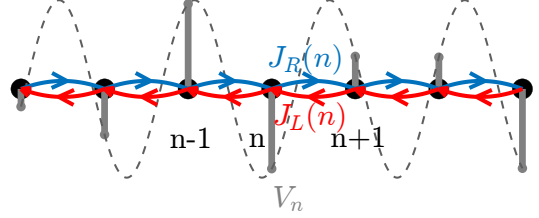


FIG. 1. Schematic of the AAH model with disordered imaginary gauge field. Blue (red) arrows indicate $J_R(n)$ [$J_L(n)$]. The gray bars depict the onsite potential V_n on each site, and the dashed curve is a guide to the quasiperiodic modulation profile.

nian reads

$$\begin{aligned} H_{\text{cont}}^H &\equiv e^{X(x)} H_{\text{cont}} e^{-X(x)} \\ &= \frac{p^2}{2m} + V_1 \sin^2(k_1 x) + V_2 \cos(2k_2 x + \varphi). \end{aligned} \quad (2)$$

In the deep-lattice regime $V_1 \gg E_R$ (with recoil energy $E_R = \hbar^2 k_1^2 / 2m$) and for a weaker secondary lattice $V_1 \gg V_2$, we project H_{cont}^H to the lowest Bloch band of the primary lattice and retain only onsite and nearest-neighbor matrix elements. Let $a \equiv \pi/k_1$ be the primary-lattice spacing and $x_n \equiv na$ the lattice sites. Expanding the field operator in lowest-band Wannier functions $w(x - x_n)$, the resulting tight-binding Hamiltonian takes the Hermitian AAH form

$$\hat{H}^H = \sum_{n=1}^N V_n \hat{c}_n^\dagger \hat{c}_n + \sum_{n=1}^{N-1} J(\hat{c}_{n+1}^\dagger \hat{c}_n + \hat{c}_n^\dagger \hat{c}_{n+1}), \quad (3)$$

where \hat{c}_n annihilates a particle on site n and N is the number of lattice sites. The nearest-neighbor hopping J is the corresponding Wannier matrix element of H_{cont}^H ; adopting the convention $J > 0$, we define $J \equiv -\int dx w(x - x_{n+1}) H_{\text{cont}}^H w(x - x_n)$, which is site-independent in the bulk for a uniform primary lattice. The onsite potential V_n is induced predominantly by the secondary lattice and is quasiperiodic,

$$V_n = \lambda \cos(2\pi\beta n + \varphi), \quad (4)$$

where the incommensurability parameter is $\beta \equiv k_2/k_1$. Within the same projection, using the localization of $w(x)$ (lowest band) and the even parity of $|w(x)|^2$, the modulation amplitude can be written as $\lambda = V_2 \int dx |w(x)|^2 \cos(2k_2 x)$, with $w(x)$ the lowest-band Wannier function of the primary lattice centered at the origin. In numerics we take β as the golden ratio.

Finally, within the tight-binding description, we restore the imaginary gauge field of the original continuum model in Eq. (1) by applying the inverse nonunitary gauge transformation to \hat{H}^H . With $X_n \equiv X(x_n)$, we define the site-diagonal operator $S = \exp(\sum_{n=1}^N X_n \hat{c}_n^\dagger \hat{c}_n)$

and obtain the non-Hermitian tight-binding Hamiltonian $\hat{H} = S\hat{H}^H S^{-1}$, i.e.,

$$\hat{H} = \sum_{n=1}^N V_n \hat{c}_n^\dagger \hat{c}_n + \sum_{n=1}^{N-1} \left[J_R(n) \hat{c}_{n+1}^\dagger \hat{c}_n + J_L(n) \hat{c}_n^\dagger \hat{c}_{n+1} \right]. \quad (5)$$

The right/left hopping amplitudes between sites n and $n+1$ are

$$J_R(n) = J e^{h_n}, \quad J_L(n) = J e^{-h_n}, \quad (6)$$

where the discrete gauge increment is

$$h_n = X_{n+1} - X_n, \quad X_1 = 0. \quad (7)$$

In what follows we focus on a Bernoulli gauge field,

$$h_n = s_n \Delta, \quad (8)$$

where $s_n = \pm 1$ is a zero-mean Bernoulli sequence and Δ controls the disorder strength [25]. The structure of the non-Hermitian AAH chain considered here is schematically illustrated in Fig. 1.

III. NONUNITARY GAUGE TRANSFORMATION AND PHASE STRUCTURE

A. Nonunitary gauge transformation

In the single-particle scenario, an eigenstate of Hamiltonian (5) can be written as $|\psi\rangle = \sum_{n=1}^N \psi_n \hat{c}_n^\dagger |0\rangle$. The coefficients ψ_n and the corresponding eigenenergy E satisfy the stationary Schrödinger equation $\hat{H}|\psi\rangle = E|\psi\rangle$, which in the site basis gives

$$J_R(n-1)\psi_{n-1} + V_n\psi_n + J_L(n)\psi_{n+1} = E\psi_n. \quad (9)$$

Using Eqs. (6) and (7), the hopping asymmetry is gauged away by the rescaling

$$\psi_n = e^{X_n} \phi_n. \quad (10)$$

Substituting Eq. (10) into Eq. (9) shows that the transformed amplitudes ϕ_n obey a Hermitian AAH equation with symmetric nearest-neighbor hopping J and on-site potential V_n ,

$$J\phi_{n-1} + V_n\phi_n + J\phi_{n+1} = E\phi_n. \quad (11)$$

Thus the entire OBC spectrum of \hat{H} coincides with that of the Hermitian AAH chain. To characterize the asymptotic spatial growth/decay of a given eigenstate in the thermodynamic limit, we introduce the Lyapunov exponent (spatial exponent)

$$\Gamma(E) = \lim_{n \rightarrow \infty} \frac{1}{n} \ln \left| \frac{\psi_n}{\psi_1} \right|. \quad (12)$$

Using Eqs. (7) and (10), one obtains the exact decomposition [25]

$$\Gamma(E) = \tilde{\Gamma}(E) + \bar{h}, \quad (13)$$

where $\tilde{\Gamma}(E)$ is the corresponding exponent extracted from ϕ_n , and

$$\bar{h} = \lim_{n \rightarrow \infty} \frac{X_n}{n} \quad (14)$$

is the spatial average of the imaginary gauge field. For the Bernoulli gauge disorder defined in Sec. II, $\bar{h} = 0$ for typical realizations in the long-chain limit, so that

$$\Gamma(E) = \tilde{\Gamma}(E). \quad (15)$$

When an eigenenergy E belonging to the continuous bulk spectrum of the Hermitian AAH chain, $\tilde{\Gamma}(E)$ is known exactly and is independent of E [26]: it vanishes for $\lambda \leq 2J$ and equals $\ln(\lambda/2J)$ for $\lambda > 2J$. Combining this result with Eq. (15), we obtain the Lyapunov exponent for bulk eigenstates of \hat{H} ,

$$\Gamma(E) = \begin{cases} 0, & \lambda \leq 2J, \\ \ln\left(\frac{\lambda}{2J}\right), & \lambda > 2J, \end{cases} \quad (16)$$

which yields the bulk localization length $\xi = 1/\Gamma$ for $\lambda > 2J$. For eigenvalues lying inside bulk gaps (e.g., edge modes under OBC), exponentially decaying solutions exist and their decay rates are generally energy dependent. Nevertheless, for any fixed eigenvalue E the nonunitary gauge transformation implies that the spatial exponent extracted from ψ_n differs from that of ϕ_n only through \bar{h} ; hence for typical zero-mean gauge realizations with $\bar{h} = 0$, the decay exponent of an in-gap state is inherited from the Hermitian counterpart.

B. ENHSE-induced collective pinning and phase diagram

To quantify the collective real-space structure of the spectrum of the non-Hermitian Hamiltonian (5), we introduce a spectrum-averaged intensity profile. Denoting the N eigenstates by $\{\psi_{\alpha,n}\}$ with eigenstate index $\alpha = 1, \dots, N$, we define

$$I_n = \frac{1}{N} \sum_{\alpha=1}^N |\psi_{\alpha,n}|^2, \quad (17)$$

which measures the eigenstate-averaged weight at site n (i.e., the average of $|\psi_{\alpha,n}|^2$ over all right eigenstates). A quantity capturing the global non-uniformity of this profile is

$$S_I = \sum_{n=1}^N I_n^2, \quad (18)$$

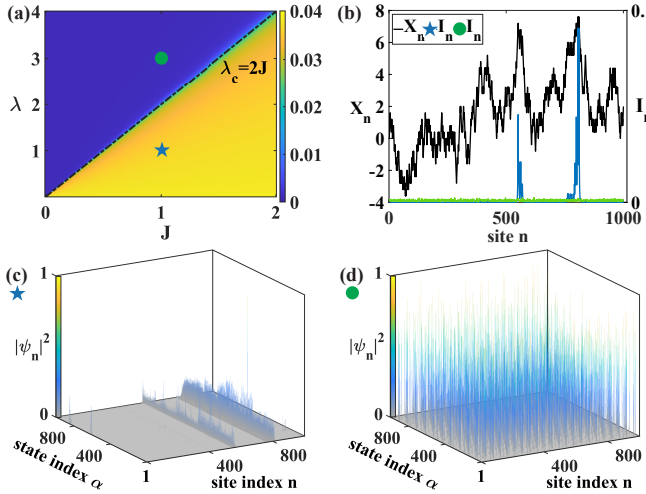


FIG. 2. Static properties and phase structure for fixed $\Delta = 0.4$, $\beta = (\sqrt{5} - 1)/2$ and $\varphi = \pi/5$ hereafter for calculations. (a) Phase diagram in the (J, λ) plane, in which $N = 1000$, color coded by S_I . The dashed line $\lambda_c = 2J$ marks the self-dual transition. The blue star and green circle indicate the parameter sets $(J, \lambda) = (1, 1)$ and $(1, 3)$, respectively. (b) Cumulative height X_n (black, left axis) and averaged intensity I_n (colored curves, right axis) for the two representative parameter sets marked in (a). (c),(d) Eigenstate density in the ENHSE regime $(J, \lambda) = (1, 1)$ and in the AAH-localized regime $(J, \lambda) = (1, 3)$, respectively.

which approaches its minimum value $S_I \simeq 1/N$ for a nearly uniform I_n , and increases when the spectral weight concentrates near a few preferred sites. Figure 2(a) shows the resulting phase diagram in the (J, λ) plane (with $N = 1000$), where the color encodes S_I . The dashed line $\lambda_c = 2J$ marks the self-dual transition inherited from the Hermitian AAH counterpart, across which the Lyapunov exponent in Eq. (16) changes from $\Gamma = 0$ to $\Gamma > 0$. In the regime $\lambda < 2J$, the Hermitian counterpart supports extended bulk eigenstates, yet the nonunitary envelope generated by the erratic imaginary gauge field can collectively concentrate the physical right eigenstates $\psi_{\alpha,n}$, yielding a strongly nonuniform I_n and hence a large S_I . In contrast, for $\lambda > 2J$ the quasiperiodic potential already localizes the eigenstates of the Hermitian counterpart, and the spectrum-averaged intensity becomes much less sensitive to the random-walk envelope, resulting in a significantly smaller S_I .

The microscopic origin of these distinct behaviors is illustrated in Fig. 2(b)–(d) for the two representative parameter sets marked in Fig. 2(a): $(J, \lambda) = (1, 1)$ (blue star, $\lambda < 2J$) and $(J, \lambda) = (1, 3)$ (green circle, $\lambda > 2J$). Figure 2(b) directly compares, for each parameter set, the cumulative random-walk profile X_n (black curve, left axis) and the spectrum-averaged intensity I_n defined in Eq. (17) (colored curve, right axis). For $(J, \lambda) = (1, 1)$, where the eigenstates of the Hermitian counterpart are extended, the nonunitary envelope e^{X_n} selects only a few preferred sites; accordingly, I_n in Fig. 2(b) devel-

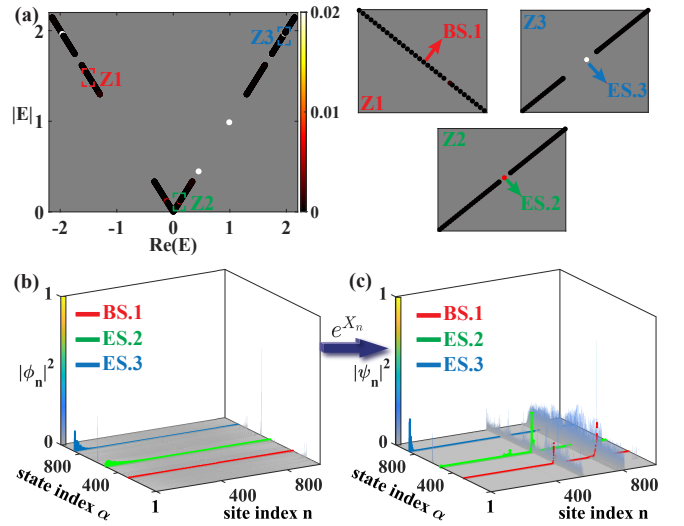


FIG. 3. Spectral and real-space structure at the parameter set indicated by the blue star marker in Fig. 2. (a) Open-boundary spectrum in the plane $(\text{Re } E, |E|)$, with color representing the Lyapunov exponent. Zoomed windows Z1, Z2, and Z3 mark the bulk state BS.1 and the in-gap states ES.2 and ES.3. In (b) and (c) eigenstates are ordered by increasing $\text{Re } E$. (b) Three-dimensional plot of the Hermitian AAH densities $|\phi_n|^2$ versus eigenstate index and site index. (c) Corresponding plot of the ENHSE-AAH densities $|\psi_n|^2$ obtained from the same eigenvalues via $\psi_n = e^{X_n} \phi_n$. In (b) and (c) the states BS.1, ES.2, and ES.3 are highlighted. Each eigenstate is normalized to unit norm.

ops sharp peaks located near the dominant maxima of X_n . This collective pinning is further corroborated by the eigenstate-density shown in Fig. 2(c), where a large fraction of the spectrum accumulates its weight around the same spatial locations. For $(J, \lambda) = (1, 3)$, by contrast, the Hermitian counterpart is in the AAH-localized regime, so individual eigenstates are exponentially localized with centers distributed across the chain. As a result, after averaging over the whole spectrum, I_n in Fig. 2(b) does not display pronounced peaks but stays close to a weakly modulated background, showing no systematic correlation with the extrema of X_n . The eigenstate-density in Fig. 2(d) directly confirms that the states remain exponentially localized with distinct localization centers, consistent with the much smaller value of S_I in this regime.

IV. COEXISTENCE OF BOUNDARY-PINNED AND GAUGE-STEERABLE EDGE STATES

With the nonunitary gauge transformation shown above, we can analyze boundary physics using the Hermitian AAH spectrum as a reference: the open-boundary eigenvalues are unchanged, and for typical zero-mean gauge realizations the spatial decay/growth exponents are inherited from the Hermitian problem. In the ENHSE

regime $\lambda < 2J$, bulk eigenstates in the continuum are extended in the Hermitian counterpart, yet exponentially decaying solutions can still occur at eigenvalues lying inside bulk gaps [26], which can be seen in Fig. 3. The gauge transformation retains the corresponding in-gap eigenvalues while reshaping their real-space profiles through the envelope e^{X_n} . Figure 3(a) shows the OBC spectrum of \hat{H} , from which we select one representative bulk state (BS.1) and two representative in-gap modes (ES.2 and ES.3), whose Hermitian counterparts are edge states for the comparison below.

Figures 3(b) and 3(c) compare the real-space distribution of all eigenstates before and after the nonunitary transformation. Fig. 3(b) shows the Hermitian AAH amplitudes $|\phi_n|^2$ as a function of eigenstate index and site index, in which BS.1 is extended along the chain, while ES.2 and ES.3 are peaked near the left boundary. Fig. 3(c) shows the corresponding ENHSE-AAH amplitudes $|\psi_n|^2$, obtained from the same eigenvalues via $\psi_n = e^{X_n} \phi_n$ for one realization of the Bernoulli sequence $\{s_n\}$. The envelope e^{X_n} leaves all eigenvalues and Lyapunov exponents unchanged but strongly reshapes the spatial profiles. For the bulk state BS.1, the transformation produces the familiar ENHSE collective pinning: the Hermitian counterpart state is extended in Fig. 3(b), while its weight in Fig. 3(c) is concentrated near the global maximum of X_n . The two in-gap modes ES.2 and ES.3 respond in a qualitatively different way. ES.3 remains localized at the edge before and after the transformation: its main peak is always pinned to the left boundary and only its tail is slightly distorted by the envelope. In contrast, ES.2 in Fig. 3(c) is pulled away from the left edge and re-centered at an interior position within the bulk, where X_n develops a local maximum. Thus the transformation of ES.2 separates the two roles: the decay exponent remains the intrinsic one set by the Hermitian in-gap edge mode, while the localization center is reselected by the gauge-induced envelope e^{X_n} through the local structure of X_n .

To establish that the Hermitian modes corresponding to ES.2 and ES.3 are bona fide edge states, i.e., spectrally isolated and localized near the boundaries rather than belonging to the bulk continuum—we perform finite-size diagnostics for the Hermitian AAH chain. We start from a reference chain of size $N = 2000$ and increase N up to 20000 in steps of $\Delta N = 500$, keeping $(J, \lambda, \beta, \varphi)$ fixed. We monitor how the in-gap eigenvalues within the windows Z2 (ES.2) and Z3 (ES.3) in Fig. 3(a) evolve with the system size N . Figures 4(a) and 4(b) show that the tracked eigenvalues of ES.2 and ES.3 remain inside bulk gaps and do not merge into the neighboring continua as N increases, indicating spectral isolation in the thermodynamic limit. To quantify boundary localization of an eigenstate ϕ_n , we compute the boundary weight

$$P_{\text{edge}} = \sum_{n=1}^{n_b} |\phi_n|^2 + \sum_{n=N-n_b+1}^N |\phi_n|^2, \quad (19)$$

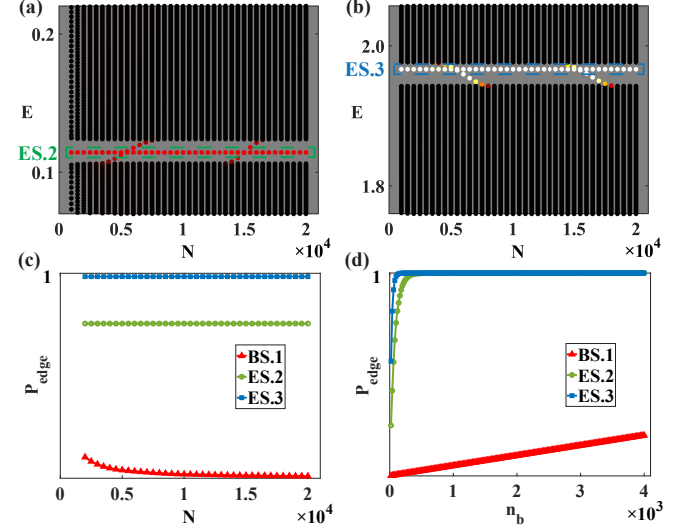


FIG. 4. Finite-size diagnostics of the three reference eigenstates in the Hermitian counterpart at $J = \lambda = 1$, $\beta = (\sqrt{5} - 1)/2$, and $\varphi = \pi/5$. (a) Eigenenergies in the gap hosting ES.2 as a function of the system size N , with the tracked ES.2 branch highlighted. (b) Same as (a) but for the gap hosting ES.3. (c) Boundary weight P_{edge} of BS.1, ES.2, and ES.3 versus N evaluated with a fixed boundary window length $n_b = 100$. (d) Boundary weight P_{edge} of BS.1, ES.2, and ES.3 versus the boundary window size n_b at $N = 40000$.

where n_b is the window length measured from each boundary. As shown in Fig. 4(c), at fixed $n_b = 100$ the boundary weight P_{edge} of the bulk reference state BS.1 decreases as the system size N increases. By contrast, the P_{edge} values of ES.2 and ES.3 are independent of N , consistent with boundary localization. This interpretation is further supported by Fig. 4(d): at fixed $N = 40000$, the boundary weights of ES.2 and ES.3 rapidly approach unity as n_b increases, whereas BS.1 remains far from saturation. Together, these finite-size diagnostics establish that the Hermitian counterparts of ES.2 and ES.3 are bona fide edge states in the thermodynamic limit. The nonunitary gauge transformation then guarantees that the corresponding OBC eigenvalues are unchanged, while the associated right/left eigenfunctions are reshaped by the gauge-induced envelope, which can shift the probability maximum of ES.2 without altering its in-gap eigenvalue.

The distinct responses of ES.2 and ES.3 to the gauge envelope are robust against changes in the ENHSE realization. To test robustness against the ENHSE realization, we keep $(J, \lambda, \beta, \varphi)$ fixed and vary only the Bernoulli sequence $\{s_n\}$. Figure 5 shows representative densities $|\psi_n|^2$ of ES.2 for five independent realizations. All curves exhibit comparable exponential tails, yet their maxima shift over the chain, tracking prominent local maxima of the cumulative gauge profile X_n . In contrast, the companion edge mode ES.3 remains essentially pinned to the boundary across realizations. Accordingly, we refer to ES.2 as a gauge-steerable in-gap mode: its localization

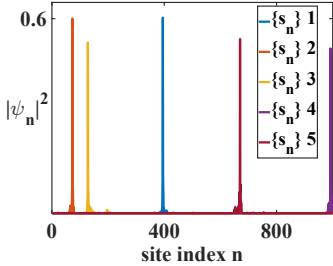


FIG. 5. Real-space probability densities $|\psi_n|^2$ of the in-gap state ES.2 for five independent realizations of the Bernoulli sequence $\{s_n\}$. All microscopic parameters are identical to those used for ES.2 in Fig. 3, only the random sequence $\{s_n\}$ is changed. Each curve corresponds to one realization.

center can be repositioned by changing the imaginary-gauge configuration, whereas ES.3 behaves as a conventional boundary pinned edge mode that is largely insensitive to the gauge randomness.

V. LOCAL-GAIN PROTOCOL FOR PREPARING THE GAUGE-STEERABLE IN-GAP STATE

We now show how to selectively prepare the gauge-steerable in-gap mode ES.2 from a bulk initial wave packet by adding weak on-site gain at a single site. The selection mechanism is set by the biorthogonal response of an isolated eigenmode to a local perturbation: for weak gain, the mode with the largest positive imaginary energy shift becomes dominant in the long-time normalized dynamics. Below we show that, for the present model, the relevant biorthogonal weight can be evaluated from the Hermitian reference problem, which fixes the gain site independently of the erratic-gauge realization.

Let $\{|\psi_\alpha^R\rangle\}$ and $\{|\psi_\alpha^L\rangle\}$ be the right and left eigenstates of \hat{H} ,

$$\hat{H}|\psi_\alpha^R\rangle = E_\alpha|\psi_\alpha^R\rangle, \quad (20)$$

$$\hat{H}^\dagger|\psi_\alpha^L\rangle = E_\alpha^*|\psi_\alpha^L\rangle, \quad (21)$$

with biorthogonal normalization $\langle\psi_\alpha^L|\psi_\beta^R\rangle = \delta_{\alpha\beta}$. Consider a local on-site perturbation applied at lattice site n ,

$$\delta\hat{V} = \delta v|n\rangle\langle n|, \quad (22)$$

where δv is the complex perturbation strength. For an isolated, nondegenerate eigenvalue E_α , first-order perturbation theory gives [44]

$$\delta E_\alpha = \langle\psi_\alpha^L|\delta\hat{V}|\psi_\alpha^R\rangle = \delta v \chi_\alpha(n), \quad (23)$$

where the biorthogonal weight is

$$\chi_\alpha(n) = \langle\psi_\alpha^L|n\rangle\langle n|\psi_\alpha^R\rangle = \psi_\alpha^{L*}(n)\psi_\alpha^R(n). \quad (24)$$

For a perturbation applied at site n , $\chi_\alpha(n)$ controls the first-order eigenvalue shift via Eq. (23). We take $\delta v = i\gamma$ with $\gamma > 0$ (on-site gain), so that $\text{Im } \delta E_\alpha = \gamma \chi_\alpha(n)$ for an isolated mode and $\gamma \ll J$. For a given target mode α , we therefore choose

$$n_0 = \arg \max_n \chi_\alpha(n), \quad (25)$$

which maximizes its gain-induced imaginary shift and makes it dominant in the long-time normalized dynamics.

Equation (10) allows one to evaluate $\chi_\alpha(n)$ from the Hermitian counterpart. Let \hat{H}^H be the Hermitian AAH Hamiltonian corresponding to \hat{H} under OBC by the nonunitary gauge transformation, and let $|\phi_\alpha\rangle$ be its normalized eigenstates,

$$\hat{H}^H|\phi_\alpha\rangle = E_\alpha|\phi_\alpha\rangle, \quad \langle\phi_\alpha|\phi_\beta\rangle = \delta_{\alpha\beta}. \quad (26)$$

The right/left eigenstates of \hat{H} are then

$$|\psi_\alpha^R\rangle = S|\phi_\alpha\rangle, \quad |\psi_\alpha^L\rangle = (S^{-1})^\dagger|\phi_\alpha\rangle, \quad (27)$$

with S diagonal in the site basis. It follows immediately that

$$\chi_\alpha(n) = \psi_\alpha^{L*}(n)\psi_\alpha^R(n) = |\phi_\alpha(n)|^2. \quad (28)$$

Therefore the optimal gain site is fixed by the profile of the Hermitian mode and is independent of the erratic-gauge realization.

We now implement the gain-selection rule for the gauge-steerable in-gap state ES.2. Let $|\phi_{\text{ES.2}}\rangle$ denote the corresponding Hermitian eigenstate (with eigenvalue $E_{\text{ES.2}}$) identified in Sec. IV. From Eq. (28) we obtain

$$\chi_{\text{ES.2}}(n) = |\phi_{\text{ES.2}}(n)|^2. \quad (29)$$

The resulting $\chi_{\text{ES.2}}(n)$ is shown in Fig. 6(a), where it attains its maximum at $n = 18$; according to Eq. (25), we therefore set the gain site to $n_0 = 18$. With n_0 fixed, we introduce weak local gain and define

$$\hat{H}_{\text{eff}} = \hat{H} + i\gamma|n_0\rangle\langle n_0|. \quad (30)$$

The gain term breaks the exact nonunitary gauge transformation in Sec. III; however, for $\gamma \ll J$ it produces only a small perturbation to the eigenstates, while shifting the eigenvalues according to the biorthogonal weight. In particular, the targeted mode acquires the largest positive imaginary shift,

$$\text{Im } \delta E_{\text{ES.2}} = \gamma \chi_{\text{ES.2}}(n_0). \quad (31)$$

With our choice of n_0 , ES.2 receives a parametrically larger positive imaginary shift than the remaining modes, as shown in Fig. 6(b), and therefore dominates the long-time normalized dynamics.

The dynamics is governed by

$$i\frac{d}{dt}|\Psi(t)\rangle = \hat{H}_{\text{eff}}|\Psi(t)\rangle. \quad (32)$$

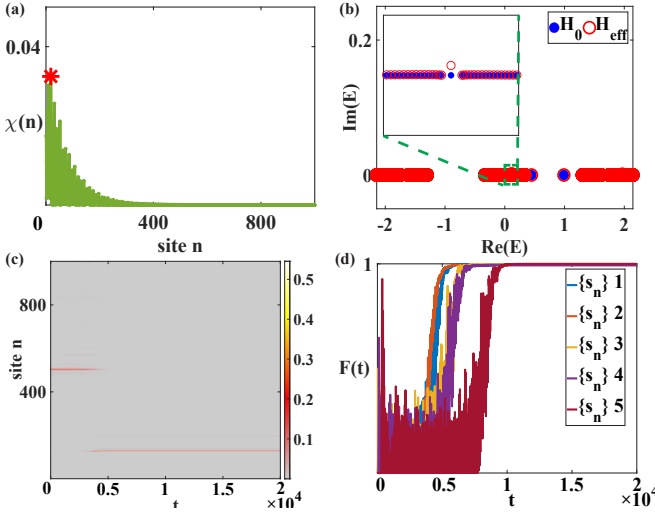


FIG. 6. (a) Biorthogonal weight $\chi_{\text{ES.2}}(n)$; the star marks the gain site $n_0 = 18$. (b) Complex spectra of \hat{H} (blue) and \hat{H}_{eff} (red), with a zoom into the gap containing ES.2. (c) Space-time map of the normalized density under \hat{H}_{eff} for a representative disorder realization, starting from a bulk-centered Gaussian wave packet. (d) Fidelity with respect to ES.2 versus time for five disorder realizations.

We numerically evolve Eq. (32); to remove the trivial overall amplification/decay inherent to non-Hermitian dynamics, the state is normalized to unit norm during the time evolution. As the initial condition we use a normalized Gaussian wave packet centered in the bulk,

$$\Psi_n(0) \propto \exp\left[-\frac{(n - n_c)^2}{2\sigma^2}\right], \quad n_c = \frac{N+1}{2}, \quad (33)$$

with $\sigma = 20$. To verify that the dynamics prepares ES.2, we monitor the fidelity with respect to the ES.2 right eigenstate,

$$F(t) = |\langle \psi_{\text{ES.2}}^{\text{R}} | \Psi(t) \rangle|^2, \quad (34)$$

where $|\psi_{\text{ES.2}}^{\text{R}}\rangle$ is the normalized ES.2 right eigenstate of Hamiltonian (5).

Figure 6(c) shows the evolution for realization 2 of the Bernoulli sequence $\{s_n\}$ (the same labeling as in Fig. 5). Starting from the bulk, the normalized profile gradually transfers to the left boundary region and converges to a sharply localized profile whose maximum coincides with the ENHSE-steered peak position of ES.2 for that realization. The fidelity in Fig. 6(d) increases from $F(0) \ll 1$ and saturates close to unity, indicating that the weak local gain preferentially amplifies the ES.2 component. We

repeat the same protocol for the five independent ENHSE realizations used in Fig. 5. For each realization, the gain site is kept fixed at the same n_0 determined once from the Hermitian counterpart, while the long-time peak position follows the realization-dependent envelope e^{X_n} . The fidelities in Fig. 6(d) all saturate near unity, demonstrating that the preparation protocol is robust to ENHSE randomness and yields a dynamically selected, position-tunable in-gap mode.

VI. CONCLUSION

We have studied a quasiperiodic non-Hermitian AAH chain with a zero-mean, spatially fluctuating imaginary gauge field. Under OBC, the model was similarity-equivalent to the Hermitian AAH chain, so the OBC spectrum was preserved while the right/left eigenstates acquired a realization-dependent random-walk envelope. In gaps that host isolated boundary modes in the Hermitian reference problem, we found two in-gap modes with distinct responses: one remained boundary pinned, whereas the other was gauge steerable, with its probability maximum shifted by changing only the gauge realization without moving its in-gap eigenvalue. We also showed that the biorthogonal weight controlling the first-order response to a local on-site perturbation reduced exactly to the site-resolved density of the corresponding Hermitian eigenstate, which fixed the optimal gain site independently of the gauge realization and enabled a weak local-gain protocol to prepare the steerable mode from a bulk initial state. Our work uncovers an exactly tractable route to position-tunable in-gap localization in non-Hermitian quasiperiodic lattices and opens a new avenue to analytically explore erratic-gauge boundary physics with clear experimental feasibility.

ACKNOWLEDGMENTS

X.L.Z. thanks Zhi Li and Peng Zou for helpful discussions. This work was supported by the Joint Fund of Natural Science Foundation of Shandong Province (Grant No. ZR2024LLZ004), the National Natural Science Foundation of China (Grant No. 12005110), and the Natural Science Foundation of Shandong Province (Grant No. ZR2020QA078, No. ZR2023QB065, No. ZR2023MD064).

[1] C. M. Bender and S. Boettcher, Real Spectra in Non-Hermitian Hamiltonians Having \mathcal{PT} Symmetry, *Phys. Rev. Lett.* **80**, 5243 (1998).

[2] C. M. Bender, Making sense of non-Hermitian Hamiltonians, *Rep. Prog. Phys.* **70**, 947 (2007).

- [3] I. Rotter, A non-Hermitian Hamilton operator and the physics of open quantum systems, *J. Phys. A: Math. Theor.* **42**, 153001 (2009).
- [4] W. D. Heiss, The physics of exceptional points, *J. Phys. A: Math. Theor.* **45**, 444016 (2012).
- [5] R. El-Ganainy, K. G. Makris, M. Khajavikhan, Z. H. Musslimani, S. Rotter, and D. N. Christodoulides, Non-Hermitian physics and \mathcal{PT} symmetry, *Nat. Phys.* **14**, 11 (2018).
- [6] M.-A. Miri and A. Alù, Exceptional points in optics and photonics, *Science* **363**, eaar7709 (2019).
- [7] S. K. Özdemir, S. Rotter, F. Nori, and L. Yang, Parity-time symmetry and exceptional points in photonics, *Nat. Mater.* **18**, 783 (2019).
- [8] C. E. Rüter, K. G. Makris, R. El-Ganainy, D. N. Christodoulides, M. Segev, and D. Kip, Observation of parity-time symmetry in optics, *Nat. Phys.* **6**, 192 (2010).
- [9] A. Regensburger, C. Bersch, M.-A. Miri, G. Onishchukov, D. N. Christodoulides, and U. Peschel, Parity-time synthetic photonic lattices, *Nature* **488**, 167 (2012).
- [10] H. Hodaei, A. U. Hassan, S. Wittek, H. Garcia-Gracia, R. El-Ganainy, D. N. Christodoulides, and M. Khajavikhan, Enhanced sensitivity at higher-order exceptional points, *Nature* **548**, 187 (2017).
- [11] L. Feng, R. El-Ganainy, and L. Ge, Non-Hermitian photonics based on parity-time symmetry, *Nat. Photon.* **11**, 752 (2017).
- [12] E. J. Bergholtz, J. C. Budich, and F. K. Kunst, Exceptional topology of non-Hermitian systems, *Rev. Mod. Phys.* **93**, 015005 (2021).
- [13] Y. Ashida, Z. P. Gong, and M. Ueda, Non-Hermitian physics, *Adv. Phys.* **69**, 249 (2020).
- [14] X. Zhang, T. Zhang, M. H. Lu, and Y. F. Chen, A review on non-Hermitian skin effect, *Adv. Phys. X* **7**, 2109431 (2022).
- [15] N. Okuma, and M. Sato, Non-Hermitian topological phenomena: A review, *Annu. Rev. Condens. Matter Phys.* **14**, 83 (2023).
- [16] S. Y. Yao and Z. Wang, Edge states and topological invariants of non-Hermitian systems, *Phys. Rev. Lett.* **121**, 086803 (2018).
- [17] F. K. Kunst, E. Edvardsson, J. C. Budich, and E. J. Bergholtz, Biorthogonal bulk-boundary correspondence in non-Hermitian systems, *Phys. Rev. Lett.* **121**, 026808 (2018).
- [18] Z. P. Gong, Y. Ashida, K. Kawabata, K. Takasan, S. Higashikawa, and M. Ueda, Topological phases of non-Hermitian systems, *Phys. Rev. X* **8**, 031079 (2018).
- [19] K. Yokomizo and S. Murakami, Non-Bloch band theory of non-Hermitian systems, *Phys. Rev. Lett.* **123**, 066404 (2019).
- [20] K. Kawabata, K. Shiozaki, M. Ueda, and M. Sato, Symmetry and topology in non-Hermitian physics, *Phys. Rev. X* **9**, 041015 (2019).
- [21] N. Okuma, K. Kawabata, K. Shiozaki, and M. Sato, Topological origin of non-Hermitian skin effects, *Phys. Rev. Lett.* **124**, 086801 (2020).
- [22] T. E. Lee, Anomalous edge state in a non-Hermitian lattice, *Phys. Rev. Lett.* **116**, 133903 (2016).
- [23] N. Hatano and D. R. Nelson, Localization transitions in non-Hermitian quantum mechanics, *Phys. Rev. Lett.* **77**, 570 (1996).
- [24] N. Hatano and D. R. Nelson, Vortex pinning and non-Hermitian quantum mechanics, *Phys. Rev. B* **56**, 8651 (1997).
- [25] S. Longhi, Erratic Non-Hermitian Skin Localization, *Phys. Rev. Lett.* **134**, 196302 (2025).
- [26] S. Aubry and G. André, Analyticity breaking and Anderson localization in incommensurate lattices, *Ann. Israel Phys. Soc.* **3**, 18 (1980).
- [27] P. G. Harper, Single band motion of conduction electrons in a uniform magnetic field, *Proc. Phys. Soc. A* **68**, 874 (1955).
- [28] D. R. Hofstadter, Energy levels and wave functions of Bloch electrons in rational and irrational magnetic fields, *Phys. Rev. B* **14**, 2239 (1976).
- [29] M. Kohmoto, Metal-insulator transition and scaling for incommensurate systems, *Phys. Rev. Lett.* **51**, 1198 (1983).
- [30] D. J. Thouless, Quantization of particle transport, *Phys. Rev. B* **27**, 6083 (1983).
- [31] Y. E. Kraus, Y. Lahini, Z. Ringel, M. Verbin, and O. Zilberberg, Topological states and adiabatic pumping in quasicrystals, *Phys. Rev. Lett.* **109**, 106402 (2012).
- [32] Y. E. Kraus and O. Zilberberg, Topological equivalence between the Fibonacci quasicrystal and the Harper model, *Phys. Rev. Lett.* **109**, 116404 (2012).
- [33] A. Celi, P. Massignan, J. Ruseckas, N. Goldman, I. B. Spielman, G. Juzeliūnas, and M. Lewenstein, Synthetic gauge fields in synthetic dimensions, *Phys. Rev. Lett.* **112**, 043001 (2014).
- [34] Y. Lahini, R. Pugatch, F. Pozzi, M. Sorel, R. Morandotti, N. Davidson, and Y. Silberberg, Observation of a localization transition in quasiperiodic photonic lattices, *Phys. Rev. Lett.* **103**, 013901 (2009).
- [35] M. Verbin, O. Zilberberg, Y. E. Kraus, Y. Lahini, and Y. Silberberg, Observation of topological phase transitions in photonic quasicrystals, *Phys. Rev. Lett.* **110**, 076403 (2013).
- [36] G. Roati, C. D'Errico, L. Fallani, M. Fattori, C. Fort, M. Zaccanti, G. Modugno, M. Modugno, and M. Inguscio, Anderson localization of a non-interacting Bose-Einstein condensate, *Nature* **453**, 895 (2008).
- [37] M. Schreiber, S. S. Hodgman, P. Bordia, H. P. Lüschen, M. H. Fischer, R. Vosk, E. Altman, U. Schneider, and I. Bloch, Observation of many-body localization of interacting fermions in a quasirandom optical lattice, *Science* **349**, 842 (2015).
- [38] S. Ganeshan, J. H. Pixley, and S. D. Sarma, Nearest neighbor tight binding models with an exact mobility edge in one dimension, *Phys. Rev. Lett.* **114**, 146601 (2015).
- [39] S. Longhi, Phase transitions in a non-Hermitian Aubry-André-Harper model, *Phys. Rev. B* **103**, 054203 (2021).
- [40] Q. B. Zeng, Y. B. Yang, and Y. Xu, Topological phases in non-Hermitian Aubry-André-Harper models, *Phys. Rev. B* **101**, 020201(R) (2020).
- [41] X. M. Cai, Localization and topological phase transitions in non-Hermitian Aubry-André-Harper models with p -wave pairing, *Phys. Rev. B* **103**, 214202 (2021).
- [42] S. Z. Li, X. J. Yu, and Z. Li, Emergent entanglement phase transitions in non-Hermitian Aubry-André-Harper chains, *Phys. Rev. B* **109**, 024306 (2024).
- [43] L. Z. Tang, G. Q. Zhang, L. F. Zhang, and D. W. Zhang, Localization and topological transitions in non-

Hermitian quasiperiodic lattices, Phys. Rev. A **103**, 033325 (2021).

[44] H. Y. Bai, Y. Chen, T. Y. Zhang, G. C. Guo, M. Gong, and X. F. Ren, Skin modes tunability and self-healing effect in photonic Floquet lattices, arXiv:2507.04085 (2025).